Space-Time Folding of the Wake Produced by a Supervelocity Rotating Point Source

Chloé d'Hardemare,[1] Sander Wildeman,[1,2] Antonin Eddi,[2] and Emmanuel Fort[1,*]
[1]Institut Langevin, ESPCI Paris, PSL University, CNRS, 1 rue Jussieu, 75005 Paris, France
[2]Laboratoire de Physique et Mécanique des Milieux hétérogenes (PMMH), CNRS, ESPCI Paris, PSL Research University, Sorbonne Université, Université Paris Diderot, 10 rue Vauquelin, 75005 Paris, France

(Received 11 October 2018; published 13 March 2019)

Wave sources moving faster than the waves they emit create a wake whose topological features are directly related to the geometry of the source trajectory. These features can be understood by considering space-time surfaces representing past emitted wave fronts. Specifically, for a supervelocity source moving along a circular path the space-time envelope folds and a cusp appears on the inner part of the wake. As a result, the wake is ultimately contained within two parallel corotating spiraling branches. In this Letter we take advantage of the low phase speed of water waves to study experimentally supervelocity sources moving at velocities up to several time the wave speed. We image in real time their emission patterns and characterize the topological features of their wakes.

DOI: 10.1103/PhysRevLett.122.104301

A perturbation moving in a medium at a constant speed along a straight path only radiates waves when its speed exceeds the phase speed of the waves in the medium. In the context of electromagnetic waves these superluminal sources are the origin of the well-known Cherenkov effect occurring when a particle enters a medium with a speed exceeding the phase speed of light in that medium. This effect was first hypothesized by Heaviside [1] and Sommerfeld [2] and was later observed and explained theoretically in the 1930s [3,4]. In acoustics, supersonic radiation—referred to as Mach waves—has been known for a long time [5–7].

A source moving on a circular trajectory will radiate even if it travels slower than the wave speed in the medium [8]. However, even in this case the nature of the radiation pattern changes drastically when the source speed exceeds that of the waves [8,9]. The topological features of the wake produced by such a rotating supervelocity source have been studied theoretically in detail [10–14], but only a handful of experimental investigations exists [5,15,16].

Objects moving with sufficient speed on the water surface leave a wake of waves behind them [17,18]. Kelvin first described the shape of the wake behind a moving object [19]. He showed that if all the wavelengths are equally radiated then the wake has an aperture angle equal to $\sin^{-}1(1/3) \simeq 19.47$ independent of the source speed. However, the aperture angle of the wake created by a finite range of wavelengths can follow a Mach-like relation in some regime [20]. Here, we take advantage of the low phase speed of gravitocapillary water waves to study a supervelocity source moving on a circular path up to several times faster than the waves. We use a real-time full-field imaging method of the water surface to visualize and characterize the features of the wake produced by such a source.

Supervelocity wake and topological features.—We start by deriving the shape of the wake for a source moving in a nondispersive medium. Although gravitocapillary waves are dispersive we will show that this theoretical framework is still relevant to our experiment due to a combined effect of the disturbance size, the water depth, and periodicity-induced resonances. The wake produced by such a source can be constructed by drawing expanding circular wave fronts emerging from each point $(x_s(t), y_s(t))$ along its past trajectory. The current contour (x, y) of a wave front radiated at time $t \leq 0$ and propagating at phase speed c is then given by $F(x, y, t) = 0$, where

$$F(x, y, t) = (x - x_s(t))^2 + (y - y_s(t))^2 - (ct)^2. \quad (1)$$

This equation corresponds to a space-time surface with coordinates (x, y, t). The wake is defined as the locus where subsequent wave fronts are tangent. In other words, these points simultaneously satisfy $F(x, y, t) = 0$ and $\partial F/\partial t = 0$. Geometrically they correspond to points of the space-time surface where the normal is orthogonal to the time axis.

We consider a source moving on a circle of radius R with angular frequency Ω. We define its Mach number as the ratio between the speed of the source and the speed of the radiated waves: $\mathrm{Ma} = R\Omega/c$. Figures 1(a) and 1(b) show examples of space-time surfaces for a source rotating at Mach numbers $\mathrm{Ma} = 0.5$ and $\mathrm{Ma} = 4$, respectively. As expected, the shape of these surfaces is a cone directed along the time axis with the apex located at the current position of the source. The cone section undergoes a helical undulation along the time axis, following the trajectory of the source. Points which satisfy the above wake conditions appear only when the undulations become strong enough to fold the surface, i.e., for $\mathrm{Ma} \geq 1$. One can obtain the

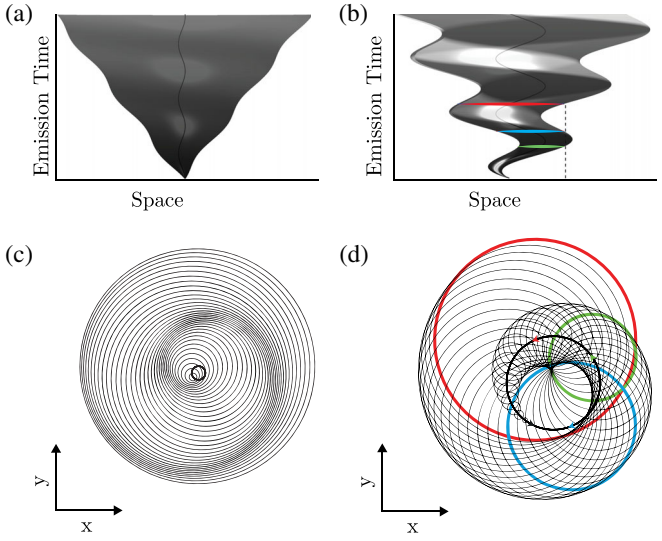

FIG. 1. (a) and (b) Surfaces composed of the past wave fronts emitted by a source moving along a circular path at Mach numbers Ma = 0.5 and Ma = 4, respectively. Inner black lines show the space-time trajectories of the source. (c) and (d) are projections along the time direction of cones (a) and (b), respectively. Only wave fronts emitted periodically are represented. Thick black circles are the source trajectories. The dashed line marks the position of an observer. Wave fronts intersecting at this position are highlighted. Positions and directions of propagation of the associated images are given by the corresponding arrows.

envelope of the wave field by projecting the cone along the time direction on the (x, y) plane as shown in Figs. 1(c) and 1(d). For better visualization, we show only wave fronts that are equally spaced in time. At Ma $>$ 1—contrary to Ma = 0.5—the folding results in a wake composed of an inner and an outer branch. The outer one simply spirals away from the trajectory. The inner one undergoes an axial reflection, forming a cusp and exits the source trajectory in a spiral similar to the outer one.

For a source rotating at Ma $\geq$ 1, the wake condition leads to the following parametric curves describing the two wake branches [11,21]:

$$x_W(\psi) = x_s + \frac{R\psi}{\mathrm{Ma}^2}\left[\sin(\psi) \pm \sqrt{\mathrm{Ma}^2 - 1}\cos(\psi)\right],$$
$$y_W(\psi) = y_s + \frac{R\psi}{\mathrm{Ma}^2}\left[-\cos(\psi) \pm \sqrt{\mathrm{Ma}^2 - 1}\sin(\psi)\right], \quad (2)$$

where $\psi = \Omega t \leq 0$. The points of the wake associated with the parameter ψ have been generated by the source at time t. The "$-$" (respectively, "$+$") sign refers to the outer (respectively, inner) branch of the envelope. The cusp occurs at $\psi_{\mathrm{cusp}} = -\sqrt{\mathrm{Ma}^2 - 1}$, where the curvature of the internal branch diverges [12]. It follows that the cusp moves on a circle with radius $R_{\mathrm{cusp}} = R/\mathrm{Ma}$ at the speed of the waves c. This circle is geometrically related to the spiraling branches of the wake [22]. The inner and outer spiraling branch can be superimposed by a rotation around the center of the trajectory. The rotation angle α_{wake} can be computed from the value of the parameter $\psi_{\mathrm{wake}} = 2\psi_{\mathrm{cusp}}$ at which the inner spirals exits the source trajectory.

Each wave front is associated with a past position of the source. For $M \leq 1$, only one wave front reaches the observer at any given time [see Fig. 1(c)], the observer thus only sees one image of the source. For Ma $>$ 1, as the source rotates, an observer standing outside of the source trajectory observes the following sequence. (i) A single image rotates in the same direction as the source. (ii) A second image appears as the outer branch of the wakes reaches her. (iii) The new image splits into two images moving in opposite directions; see observer in Figs. 1(b)–1(d). Intersecting wave fronts are highlighted and the arrows indicate the perceived propagation direction of the images. (iv) The initial image merges with the contrapropagating one as the inner branch of the wake reaches the observer. (v) The merged images disappear, leaving one image propagating in the direction of the source. The sequence repeats itself with the period of the source, $2\pi/\Omega$. The appearance and disappearance of the images can be well understood in the framework of catastrophe theory [10,23,24].

Experimental setup.—A schematic of the experimental setup is presented in Fig. 2(a). A square plexiglass tank with a base area of 50×50 cm^2 is filled to a height $h_0 = 1$ cm of deionized water. The source consists of a needle with a nozzle diameter of 0.51 mm placed at the end of a rotating horizontal tube. The needle is oriented vertically and set 1 cm above the water surface. A controlled air flow led through the needle locally indents the water surface. The flow rate is controlled by a tunable mass flow meter. Typical flow rate used for the experiments is 0.31 L min^{-1}. The source moves along a circular path with radii R ranging from 3 to 5 cm. Rotation frequencies Ω range between 6 and 36 rad s^{-1}.

We measure the wave fields using a quantitative real-time full-field measurement method [25]. A checkerboard pattern is set beneath the plexiglass tank at a distance of 7 cm. A CCD camera (acA2040-90um–Basler ace) recording at 90 fps set above of the bath records 2048×2048 px^2 images of the full tank with a resolution of $\sim$247 μm px^{-1}. We reconstruct the surface elevation with a vertical resolution of 3 μm.

Figure 2(b) shows the experimental profile of the water surface (solid line) as a function of the radial distance r obtained for a still pressure source. The dip has a typical FWHM width of 7 mm and a depth of 0.09 mm. Following Ref. [26], we use a Gaussian expression for the pressure distribution at the surface $P_{\mathrm{ext}}(r) = P_0 \exp[-2(r/d)^2]$ where d is the nozzle diameter. The experimental profile of the water surface is related to the pressure distribution by [27]: $\omega^2(k)\hat{\zeta}(k) = k\hat{P}_{\mathrm{ext}}(k)/\rho$. The right-hand term of the

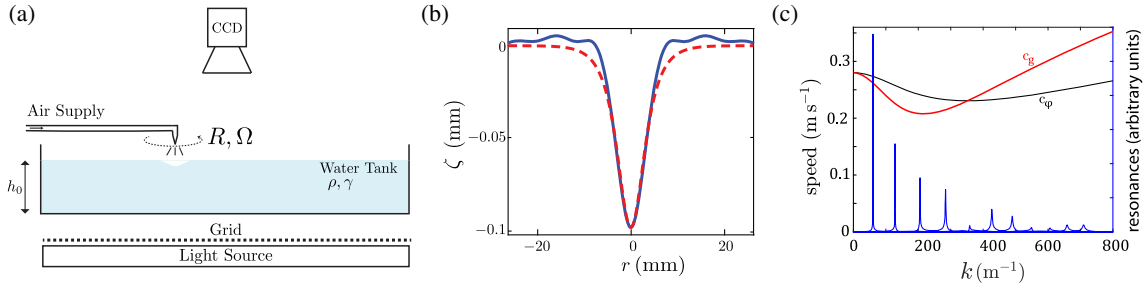

FIG. 2. (a) Schematic of the experimental setup. A pressure source is moving on a circular path over a tank filled with $h_0 = 1$ cm of water. (b) Experimental profile of the cavity formed on the water surface (solid line) by a still and steady pressure source and profile (dashed line) computed from the Gaussian fit of the pressure profile. (c) Left axis. Phase (c_ϕ) and group (c_g) speed of the waves as a function of the wave number k obtained from Eq. (3). Right axis. Weights (bracket term in Eq. (4) of the Bessel functions $J_n(kr)$ in terms of which we decompose the field. To each peak corresponds an order n ranging from 1 to 11 (from left to right). Amplitudes are given in arbitrary units.

equation is the source term for the field on the surface. We fit the experimental surface profile ζ based on the equation with $P_0 = 0.247$ N m^{-2} as the value of the fitting parameter. The dashed line in Fig. 2(b) shows the result of the fit. The model is in very good agreement with the experimental profile. Low amplitude (~ 10 μm) capillary waves are visible on the experimental curve. They are emitted by small oscillations of the bottom and sides of the air cavity [26,28].

Water wave emission model.—A disturbance moving on the water surface radiates a wave packet composed of a superposition of wavelengths. For water waves, the dispersion relation is given by [29]:

$$\omega(k)^2 = \left(gk + \frac{\gamma k^3}{\rho}\right)\tanh(kh_0), \tag{3}$$

where k is the wave number, g is the gravitational acceleration, γ the water surface tension (0.072 N m^{-1}), ρ its density (1000 kg m^{-3}), and h_0 is the liquid depth. Figure 2(c) shows the phase speed $c_\phi(k) = \omega/k$ and group speed $c_g = \partial\omega/\partial k$ as a function of k. The phase speed curve displays a minimum value $c_{\min} \simeq 23$ cm s^{-1}, corresponding to $k_{\min} \simeq 369$ m^{-1} and $\lambda_{\min} \simeq 1.7$ cm at the transition between gravity and capillary regimes.

We use a linear hydrodynamic model developed by Chepelianskii *et al.* to compute the wave field emitted by the rotating source [8]. In the steady state the wave field rotates at Ω along with the source. In the rotating frame, the vertical displacement in polar coordinates [(r, ϕ) with origin at the trajectory center] is given by

$$h(r,\phi) = \sum_{n=-\infty}^{+\infty} e^{in\phi} \int dk \times \left(\frac{k}{2\pi\rho}\frac{k\hat{P}_{\text{ext}}(k)J_n(kR)}{n^2\Omega^2 - \omega^2(k) + 4in\nu k^2\Omega}\right)J_n(kr), \tag{4}$$

where J_n is the nth order Bessel function of the first kind, $\nu = 10^{-6}$ m^2 s^{-1} is the water viscosity, and $\hat{P}_{\text{ext}}(k)$ is the Fourier transform of the pressure source $P_{\text{ext}}(r)$. As detailed above, the pressure source is assumed to be Gaussian with characteristic values taken from the fit of the static dip profile.

The term in brackets in the integrand in Eq. (4) exhibits resonances corresponding to harmonics of the rotation frequency. Each resonance is associated with a spatial Bessel function of order n. Figure 2(c) (right axis) shows the position and relative magnitude of the resonances (solid blue line) defined as (for $R = 3.5$ cm and $\Omega \simeq 20$ rad s^{-1}). The sharp decrease in magnitude with k is due to viscous damping for larger k. Periodicity confines the k spectrum of the field to a sharply combed pattern. Therefore, in the range of Ω of our study, the source mostly excites wavelengths such that $\lambda \gg \lambda_c$ where $\lambda_c = 2\pi(\gamma/\rho g)^{1/2}$ is the capillary length. In the case of a fast moving source this leads to a regime where the aperture angle follows a Mach-like relation with the source speed [20]. Figure 2(c) (left axis) also shows the phase speed c_ϕ and group speed c_g. The low water depth has a flattening effect at low k so that the dispersion effects are strongly reduced compared to the deep water case. The phase and group speed are very similar over the range of k relevant to our experiment. We can thus expect that the field consists of a superposition of Mach-like wakes associated with slightly different Mach numbers. In order to characterize our experiments we define a Mach number associated with the minimum phase speed as $\text{Ma}_{\min} = R\Omega/c_{\min}$.

Results and discussion.—Figure 3 shows snapshots of the experimental and corresponding numerical wave fields at Mach numbers $\text{Ma}_{\min} = 1.2$, $\text{Ma}_{\min} = 2$, and $\text{Ma}_{\min} = 3.3$ (a typical movie is provided as Supplemental Material [30]). The dashed circles show the trajectories followed by the counterclockwise rotating sources (indicated by arrows).

We find a good qualitative agreement between measured and computed wave fields for each Mach number. The

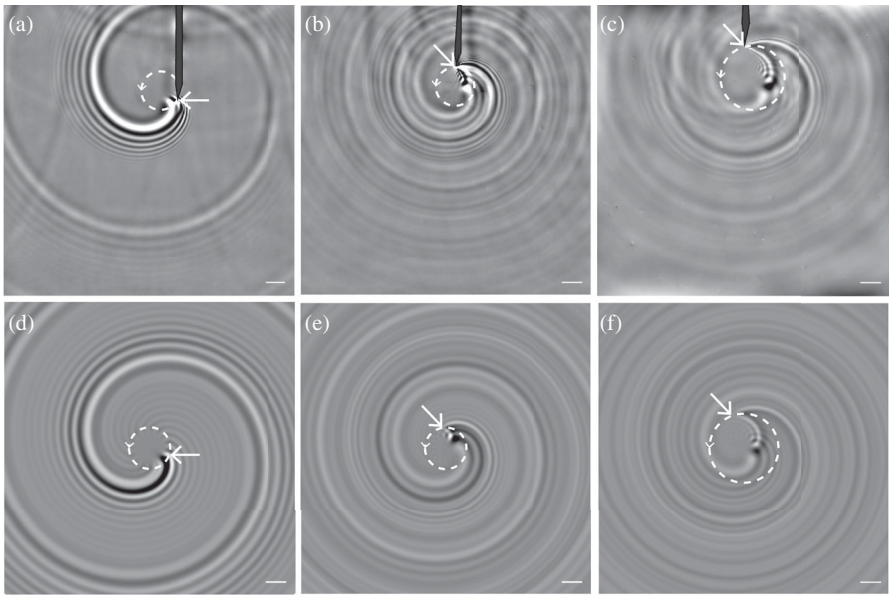

FIG. 3. (a)–(c) Experimental wave fields produced on the water surface by a pressure source moving on a circular path at $\mathrm{Ma}_{\mathrm{min}} = 1.2$, $\mathrm{Ma}_{\mathrm{min}} = 2$ and $\mathrm{Ma}_{\mathrm{min}} = 3.3$ respectively. (d)–(f) show corresponding wave fields computed from the hydrodynamic model. White oriented dashed circles depict the source trajectories while white arrows point at the current positions of the sources. 1.5 cm long white bars are superimposed on the fields for scale.

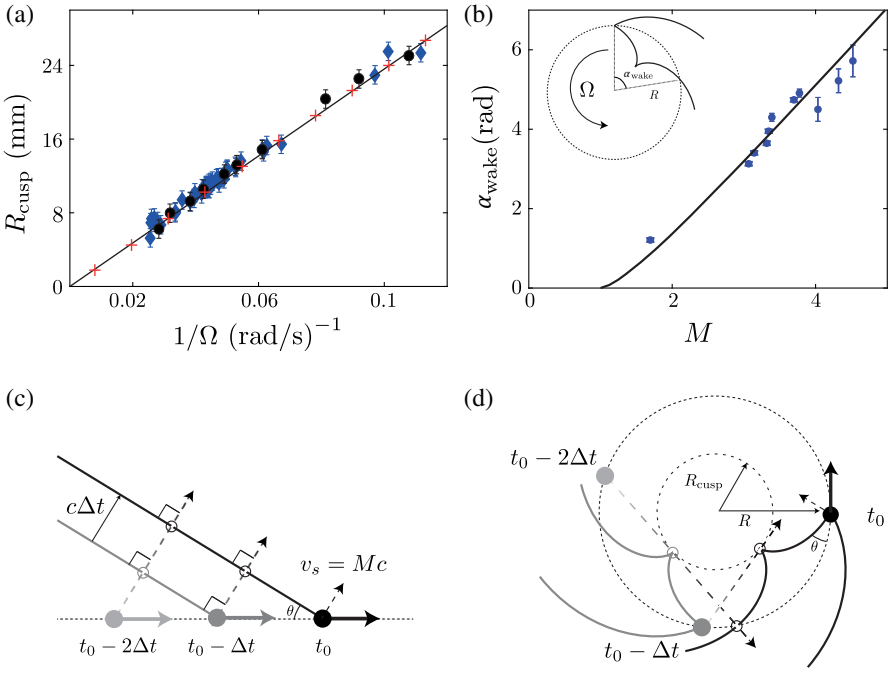

FIG. 4. (a) Radius of the cusp trajectory $R^{\mathrm{exp}}_{\mathrm{cusp}}$ as a function of the inverse of the rotation pulsation $1/\Omega$ for trajectory radii of $R = 3$ cm (blue diamonds) and $R = 5$ cm (black circles). Red crosses denote values obtained from the hydrodynamic model while the solid black line shows the analytical solution. (b) Angular distance αwake between the two branches of the spiraling wake (inset) as a function of the Mach number $\mathrm{Ma}_{\mathrm{min}}$. The solid black line gives the analytical solution. (c) Wake propagation for a source moving along a straight line. (d) Corresponding schematic in the case of a source moving on a circular path.

wake is ultimately composed of two parallel spiral branches propagating outward. The inner branch close to the source is first going inward before being reflected radially at a cusp. It never enters the circular cusp trajectory of radius $R_{\mathrm{cusp}}^{\mathrm{exp}}$. The amplitude of the waves is much smaller within this circle than within the wake. As the Mach number increases, the cusp moves inwards. Slight effects from dispersion are visible in the field as each component propagates at its own phase speed. Several shifted cusps corresponding to different wavelengths are observed for $\mathrm{Ma}_{\mathrm{min}} = 2$ and $\mathrm{Ma}_{\mathrm{min}} = 3.3$. We note that the opening angle of the wake decreases with $\mathrm{Ma}_{\mathrm{min}}$. This suggests that we indeed operate in a Mach-like regime normally associated with a dispersion-free medium.

Figure 4(a) shows the evolution of the position of the innermost cusp $R_{\mathrm{cusp}}^{\mathrm{exp}}$ as a function of $1/\Omega$ for trajectory radii $R = 3$ cm (blue diamonds) and $R = 5$ cm (black circles). Red crosses show results obtained from the hydrodynamic model while the solid black line represents the analytic solution: $R_{\mathrm{cusp}}^{\mathrm{exp}} = c_{\mathrm{min}}/\Omega$. Both experimental and numerical results are in good agreement with the analytic model. Linear fits to the data give $c_{\mathrm{min}}^{\mathrm{exp}} = 24.4\ \mathrm{cm\,s^{-1}}$ and $c_{\mathrm{min}}^{\mathrm{num}} = 23.6\ \mathrm{cm\,s^{-1}}$. Figure 4(b) shows the measured angle α_{wake} between the two spiraling branches of the wake (see inset) as a function of $\mathrm{Ma}_{\mathrm{min}}$ for $R = 3.5$ cm (blue circles). Also here the analytical model (solid line) gives a good prediction.

It is interesting to consider the wake propagation from another point of view to get some new insight on its shape and topological features. As discussed above the wake is the envelope of successive expanding wave fronts. We can use the Huygens-Fresnel principle to deduce its evolution. As an example, Fig. 4(c) shows a schematic for the propagation of one of the wake branches in the case of a supervelocity source moving along a straight line at $v_s = \mathrm{Ma}c$. One finds the envelope at a given time by simply propagating each elementary portion of the wake at previous time (hollow circles) at speed c in the direction normal to the wake (dashed arrows). The wake aperture is therefore given by the Mach angle $\theta = 0.5\ \arcsin(1/\mathrm{Ma})$.

Figure 4(d) shows the same schematic in the case of a rotating source. The source radiates in the direction orthogonal to the Mach angle. These rays are naturally tangent to a circle of radius $R_{\mathrm{cusp}} = R\sin\theta/2 = R/\mathrm{Ma}$. The ray emitted by the source at $t_0 - \Delta t$ with $\Delta t = R/c\sqrt{1 - 1/\mathrm{Ma}^2}$ reaches this circle at time t_0 where and when it forms the cusp. The portion of the wake branch comprised between the source and the cusp is formed by the rays that did not yet reach the cusp circle. The rays emitted before $t_0 - \Delta t$ form the outward spiraling part of the inner branch. In particular, the ray emitted at $t_0 - 2\Delta t$ forms the wake at the point where it exits the source trajectory at t_0. Note that this same ray formed the cusp at $t_0 - \Delta t$.

We have demonstrated experimentally the generic wake features produced by a rotating supervelocity source. The use of water wave sources enables a complete quantitative characterization of the wake shape, including the cusp position and the angular separation between the outward spiraling branches. These features result only from geometrical and topological considerations. We have interpreted them by the folding of the space-time surface composed of the previously emitted wave fronts. This folding induces the observation of simultaneous images of the source by an observer. Our study only focused on the envelope of the wave field and did not describe any interference phenomena between these images. In further studies the simpler field produced by a monochromatic wave source will allow us to focus on the specific features of the images—Doppler effect, time reversal—and the effect of interference on the radiated power [31,32].

The authors acknowledge the support of the AXA research fund and the French National Research Agency LABEX WIFI (Laboratory of Excellence ANR-10-LABX-24).

*emmanuel.fort@espci.fr

[1] O. Heaviside, Electromagnetic waves, the propagation of potential, and the electromagnetic effects of a moving charge, Electrical papers, 1888, https://archive.org/details/electricalpapers02heavrich/page/n7.
[2] A. Sommerfeld, Überlichtgeschwindigkeitsteilchen, Proc. K. Ned. Akad. Wet. **8**, 346 (1904).
[3] P. A. Cherenkov, Visible emission of clean liquids by action of γ radiation, Dokl. Akad. Nauk SSSR **2**, 451 (1934).
[4] I. Tamm and I. Frank, in *Coherent Visible Radiation of Fast Electrons Passing Through Matter* edited by B. M. Bolotovskii, V. Y. Frenkel, and R. Peierls (Springer, Berlin, 1991).
[5] W. F. Hilton, The photography of airscrew sound waves, Proc. R. Soc. Ser. A **169**, 174 (1938).
[6] H. H. Hubbard and L. W. Lassiter, Sound from a two-blade propeller at supersonic tip speeds, NACA Report No. 1079, 1952.
[7] M. V. Lowson, Focusing of helicopter BVI noise, J. Sound Vib. **190**, 477 (1996).
[8] A. D. Chepelianskii, F. Chevy, and E. Raphael, Capillary-Gravity Waves Generated by a Slow Moving Object, Phys. Rev. Lett. **100**, 074504 (2008).
[9] R. C. Vermeulen, Superluminal sources, Proc. Natl. Acad. Sci. U.S.A. **92**, 11385 (1995).
[10] H. Ardavan, The speed-of-light catastrophe, Proc. R. Soc. A **424**, 113 (1989).
[11] B. M. Bolotovskiĭ and V. P. Bykov, Radiation by charges moving faster than light, Sov. Phys. Usp. **33**, 477 (1990).
[12] B. M. Bolotovskiĭ and V. L. Ginzburg, The Vavilov-Cerenkov effect and the doppler effect in the motion of sources with superluminal velocity in vacuum, Sov. Phys. Usp. **15**, 184 (1972).

[13] R. M. Arkhipov, M. V. Arkhipov, I. V. Babushkin, and Y. A. Tolmachev, Transient radiation from a ring resonant medium excited by an ultrashort superluminal pulse, Quantum Electron. **45**, 590 (2015).
[14] M. J. Rees, Appearance of relativistically expanding radio sources, Nature (London) **211**, 468 (1966).
[15] A. Ardavan, W. Hayes, J. Singleton, H. Ardavan, J. Fopma, and D. Halliday, Experimental observation of nonspherically-decaying radiation from a rotating superluminal source, J. Appl. Phys. **96**, 4614 (2004); **96**, 7760 (2004).
[16] E. N. Snezhkin and A. M. Fridman, Over-reflection in lab: The all-sufficient cause of instability of an annular supersonic shear in simulations on free-surface shallow water, in *Proceedings of 18ème Congrès Franćais de Mécanique* (Grenoble, 2007).
[17] E. Raphaël and P.-G. De Gennes, Capillary gravity waves caused by a moving disturbance: Wave Resistance, Phys. Rev. E **53**, 3448 (1996).
[18] R. Ledesma-Alonso, M. Benzaquen, T. Salez, and E. Raphaël, Wake and wave resistance on viscous thin films, J. Fluid Mech. **792**, 829 (2016).
[19] L. Kelvin, On ship waves, Proc. Inst. Mech. Eng. **38**, 409 (1887).
[20] F. Moisy and M. Rabaud, Mach-like capillary-gravity wakes, Phys. Rev. E **90**, 023009 (2014).
[21] C. J. Chapman, The spiral Green function in acoustics and electromagnetism, Proc. R. Soc. A **431**, 157 (1990).
[22] Note that the outward-going part of the inner branch and the cusp trajectory are involute and evolute of each other, respectively.
[23] R. Thom, Stabilité structurelle et morphogénèse, Poetics **3**, 7 (1974).
[24] V. I. Arnol'd, Critical points of smooth functions and their normal forms, Russ. Math. Surv. **30**, 1 (1975).
[25] S. Wildeman, Real-time quantitative Schlieren imaging by fast Fourier demodulation of a checkered backdrop, Exp. Fluids **59**, 97 (2018).
[26] R. B. Banks and D. V. Chandrasekhara, Experimental investigation of the penetration of a high-velocity gas jet through a liquid surface, J. Fluid Mech. **15**, 13 (1963).
[27] D. Richard and E. Raphael, Capillary-gravity waves: The effect of viscosity on the wave Resistance, Europhys. Lett. **48**, 49 (1999).
[28] F. R. Cheslak, J. A. Nicholls, and M. Sichel, Cavities formed on liquid surfaces by impinging gaseous jets, J. Fluid Mech. **36**, 55 (1969).
[29] M. J. Lighthill, *Waves in Fluids* (Cambridge University Press, Cambridge, England, 2001).
[30] See Supplemental Material at http://link.aps.org/supplemental/10.1103/PhysRevLett.122.104301 for a reconstructed movie of the wavefield created by a pressure source rotating at $\mathrm{Ma} = 2.45$ (4.5-fold slow-motion acquired at 90 fps, shown at 20 fps).
[31] M. Brillouin, Actions mécaniques à hérédité discontinue par propagation, Compt. Rend. **168**, 1318 (1919).
[32] M. Brillouin, Action à heredité discontinue et raies spectrales, Compt. Rend. **171**, 1000 (1920).